Influence of surface morphology on D_2 desorption kinetics from amorphous solid water

L. Hornekær,[a] A. Baurichter, V. V. Petrunin, and A. C. Luntz
Department of Physics, University of Southern Denmark, Campusvej 55, 5230 Odense M, Denmark

Bruce D. Kay
Pacific Northwest National Laboratory, Fundamental Sciences Directorate, Chemical Sciences Division, P.O. Box 999, Mail Stop K8-88, Richland, Washington 99352

A. Al-Halabi[b]
Leiden Institute of Chemistry, Gorlaeus Laboratories, P.O. Box 9502, 2300 RA Leiden, The Netherlands

(Received 16 September 2004; accepted 12 January 2005; published online 25 March 2005)

The influence of surface morphology/porosity on the desorption kinetics of weakly bound species was investigated by depositing D_2 on amorphous solid water (ASW) films grown by low temperature vapor deposition under various conditions and with differing thermal histories. A broad distribution of binding energies of the D_2 monolayer on nonporous and porous ASW was measured experimentally and correlated by theoretical calculations to differences in the degree of coordination of the adsorbed H_2 (D_2) to H_2O molecules in the ASW depending on the nature of the adsorption site, i.e., surface valleys vs surface peaks in a nanoscale rough film surface. For porous films, the effect of porosity on the desorption kinetics was observed to be a reduction in the desorption rate with film thickness and a change in peak shape. This can be partly explained by fast diffusion into the ASW pore structure via a simple one-dimensional diffusion model and by a change in binding energy statistics with increasing total effective surface area. Furthermore, the D_2 desorption kinetics on thermally annealed ASW films were investigated. The main effect was seen to be a reduction in porosity and in the number of highly coordinated binding sites with anneal temperature due to ASW restructuring and pore collapse. These results contribute to the understanding of desorption from porous materials and to the development of correct models for desorption from and catalytic processes on dust grain surfaces in the interstellar medium. © *2005 American Institute of Physics*. [DOI: 10.1063/1.1874934]

I. INTRODUCTION

Amorphous solid water (ASW) has been studied extensively during recent years since it is considered to be a good model[1] or even a metastable extension[2] of liquid water and since it plays an important role as a catalytic surface in the interstellar medium (ISM).[3,4] ASW can be produced in several different ways: by pressurizing crystalline hexagonal ice at low temperature,[5] by hyperquenching of micrometer size water droplets,[6] and by slow vapor deposition of water on low temperature substrates.[7,8] Since ASW may exist in different states and exhibit different morphologies, it is unlikely that the detailed structure of the ASW prepared by the various methods is identical. In this paper we will limit our discussion to ASW produced by the last method, which is believed to be the one most closely resembling interstellar ices.

The morphology of ASW films grown by vapor deposition on low temperature substrates under vacuum at low deposition rates [a few monolayers/s (ML/s) or lower] is known to depend on deposition temperature, deposition rate, angular distribution of the incoming water molecules, and the thermal history of the ASW film after formation.[3,7–12] For deposition on low temperature substrates (<90 K), normal incidence water molecules produce nonporous ASW films, while off-normal incidence (or background dosing) produces porous films consisting of open networks of nanometer sized pores.[9–11] The ASW film porosity for non-normal or background dosing also depends on the growth temperature or subsequent annealing temperature of the film.[3,8,9,12] For example, dosing or annealing at substrate temperatures above 90 K reduces the porosity strongly[9] and at temperatures above 120 *K*, fully nonporous ASW structures result.[13,14] At temperatures above ~136 K crystallization into a cubic crystalline structure sets in, and at even higher temperatures the normal hexagonal crystalline ice structure is produced.[8,15] The porosity of ASW films can also be influenced by codeposition of other gases.[16]

Apart from changes in ASW film porosity with growth temperature, x-ray[7] and electron diffraction[8] experiments imply that ASW films grown at temperatures below 30 K arrange in a "local" chemical structure of higher density than ASW films grown at higher temperatures. This high density state is referred to as the high density amorphous (HDA) phase, while the low density state obtained at temperatures

[a]Present address: Institute of Physics and Astronomy, Aarhus University, Ny Munkegade Bygn. 520, 8000 Aarhus C, Denmark. Electronic mail: liv@phys.au.dk
[b]Also known as A. Al-Remawi. Present address: Surface Science Research Centre, Department of Chemistry, The University of Liverpool, Liverpool L69 3BX, UK.

above 30 K is referred to as the low density amorphous (LDA) phase.[8] Annealing ASW films in the HDA phase to temperatures above 30 K results in a slow and irreversible phase transition to the LDA phase.[8] Lately, experiments using neutron scattering[17] have failed to detect a HDA phase grown by low temperature, slow vapor deposition, while experiments using x-ray absorption spectroscopy[12] and electron-induced dissociation of CF_2Cl_2 adsorbed on an ASW surface[18] has reconfirmed it. Molecular dynamics simulations support the existence of a high density amorphous phase by showing that simulated vapor deposited amorphous ice films grown at 60 K show a structure intermediate between the high density and low density amorphous state.[19]

Infrared spectroscopy data of the dangling OH bonds of ASW films grown by background dosing at low substrate temperature shows a high absorption signal at frequencies assigned to two- and three-coordinated water molecules.[13] As the ASW film is warmed to temperatures above 60 K, the IR bands assigned to two-coordinated molecules diminish, and as the temperature is further increased, the IR bands of the three-coordinated molecules are reduced in number as well. At temperatures above 120 K, only four-coordinated water molecules are observed, corresponding to a fully hydrogen bonded H_2O solid bulk network.[13] Likewise, classical trajectory calculations of amorphous water ice clusters formed at low temperatures show the existence of two- and three-coordinated water molecules.[20–22] Simulated heating of the clusters resulted in a reduction in low coordinated molecules and an increase in three- and four-coordinated molecules. The reduction in molecules of low coordination with increasing temperature parallels that for the reduction in porosity due to annealing or growth temperature. The observed thermal evolution,[13] as well as theoretical models,[21,22] supports the interpretation that the two- and three-coordinated molecules are characteristic of H_2O molecules at the surface of the original nanometer sized pores.

Since ASW films on interstellar grains play an important role as catalytic surfaces in the low temperature environment of the ISM, a number of experiments and theoretical calculations have been carried out to study both catalytic reactions[23–28] and adsorption/desorption of atoms and molecules[3,14,29–40] on ASW surfaces. These experiments and calculations show that not only the chemical structure but also the morphology of the ASW film play a role in determining its catalytic properties[26,27] and the desorption dynamics of molecules adsorbed or created in the film.[3,14,29,30,32–35,41] For example, the fact that ASW films begin to reconstruct at relatively low temperatures, means that adsorbed molecules can become trapped in collapsing pores. The trapped gasses are then only released when the ASW film begins to crystallize at much higher temperatures, a phenomenon known as molecular volcanoes.[29,31,33]

In this paper, we present detailed temperature programmed desorption (TPD) studies of D_2 molecules adsorbed on ASW films grown at low temperatures and show that the desorption kinetics of this weakly bound species is highly dependent on ASW film morphology. More specifically we present experimental data on the D_2 desorption kinetics from ASW films grown at temperatures of 10 K and 120 K, as well as for ASW films grown at 10 K and subsequently annealed to higher temperatures. The desorption kinetics of this system, compared to the kinetics of more strongly bound adsorbates (CO, CH_4, CCl_4) studied so far, is simplified by the fact that D_2 is very weakly bound to the ASW surface. It therefore desorbs at temperatures below that where significant thermal restructuring of the ASW film occurs, e.g., pore collapse. This enables us to develop a simple model which is qualitatively able to explain the desorption kinetics of weakly bound species from porous films. We also present theoretical results of classical trajectory calculations pertaining to the sticking of H_2 on ASW and crystalline H_2O ice surfaces. Molecular dynamics simulations were performed to determine the sticking probability and the binding energy distributions of H_2 adsorbed on ASW and crystalline ice surfaces. The theoretical results are compared with those obtained from the TPD experiments.

The presented results have important implications for understanding the chemistry in dense interstellar clouds where ice covered dust grains are believed to play a decisive role. According to present models the icy mantles on interstellar dust grains are composed predominantly of water ice with other molecular species, such as CO, CH_3OH, CO_2, NH_3, CH_4, O_2, and N_2, added in varying amounts.[42,43] The majority of the water ice is formed *in situ* by recombination of hydrogen and oxygen atoms to H_2O molecules on the grain surface, rather than by condensation of H_2O molecules from the gas phase.[44] However, the absorption features of interstellar ice are well reproduced by the absorption features of ASW ice formed by vapor deposition of H_2O and kept at a temperature below 30 K.[45] Hence we believe that ASW ice films formed by low temperature vapor deposition constitute the best simple one-component model for icy mantles on interstellar grains. We have shown elsewhere[26] that the morphology of ASW films greatly influences the surface recombination of atomic hydrogen to form H_2. Most importantly the energy content of H_2 as it is released from the ASW surface into the gas phase was observed to be determined by the ASW film morphology and we also suggested that molecules desorb at a rate which is highly dependent on ASW film morphology. This last effect can be qualitatively explained by the simple model presented later. We believe that these observations have direct implications on understanding the formation of H_2 in the interstellar medium, a process considered to be one of the most important in interstellar chemistry. Also, the observed dependence of the desorption kinetics on ASW film morphology may have implications on the fate of other chemical species, such as N_2, CO, CO_2, CH_3OH, etc., formed or adsorbed on "ice" covered interstellar grains, although complications can exist from entrapment of more strongly bound species.[33]

II. EXPERIMENTAL SETUP

The general experimental setup used for the experiments reported here has been described in considerable detail elsewhere.[46] All experiments are performed in an ultrahigh vacuum (UHV) surface science chamber with a base operat-

ing pressure below 1×10^{-10} Torr. The substrate, a polished 10×10 mm^2 polycrystalline copper disk, is mounted on a Cu cold finger attached to a flowing liquid helium cryostat. Heating of the polycrystalline Cu sample is performed by electron bombardment on the backside of the Cu sample. Electrical insulation of the sample is obtained by inserting a 1 mm thick sapphire disk with a central 9 mm diameter hole between the Cu cold finger and the substrate. This also ensures good thermal contact between the cold finger and sample at low temperatures and reasonable thermal insulation at high temperatures. The sample temperature is measured by two type E (75 μm) thermocouples using a liquid N_2 temperature reference and a Keithley nanovoltmeter for the actual temperature reading. The thermocouples have been calibrated against both a silicon diode and against low temperature desorption of gas multilayers.[47] The uncertainty in the absolute temperature calibration is ±1 K. Temperature control and ramping are performed using a Eurotherm temperature controller. The entire cold finger and sample mount are surrounded by a cryogenic shield with a 6 mm diameter circular aperture centered on the sample front face. The lowest sample temperature attainable is 7 K. Before ASW film growth, the Cu sample is cleaned by ion sputtering (Ar, 2 keV) and thermal annealing to 650 K. Deionized H_2O, purified by a series of freeze-thaw cycles, is dosed onto the Cu substrate from a capillary array doser positioned 5 mm from the sample surface with a ~45° half-width at half-maximum angular spread as judged by the ASW pattern on the cryoshield. Typical dose rates are 0.3–3 ML/s. Under these H_2O deposition conditions and a surface temperature of $T_s \leqslant 10$ K, modestly porous ASW films are grown. Based on the angular distribution and the temperature of the sample we estimate a porosity of $\xi_{por}\simeq0.1$ (where ξ_{por} is defined as the percentage increase in internal surface area per monolayer of ASW relative to the external surface area of the film),[10] however, this estimate is somewhat uncertain. Although we have not made any independent studies on the nature of the porous distribution, we certainly anticipate that this forms a three-dimensional interconnected network as observed previously[9] and predicted by ballistic growth models.[11] With H_2O deposition at $T_s=120$ K, nonporous ASW films are grown.[9] According to Ref. 8 the ASW films grown at 10 K will be in the high densitity phase, while the ASW films grown at 120 K will be in the low density phase. Calibration of the ASW film thickness is made by comparing integrated water TPD signals to the integrated TPD signal obtained from the water bilayer on a single crystal Pt (111) surface of the same surface area.

D_2 molecules are dosed onto the sample from a 300 K thermal molecular beam originating from a triply differentially pumped beam line. The 1.5 mm diameter beam is directed at the center of the ASW film at normal incidence. The typical flux employed is 10^{13} cm^{-2} s^{-1} or ≃0.01 ML/s. All molecular beam doses are given as equivalent monolayer (ML) exposures, although it must be accepted that this is only approximately known due to the uncertainty in the absolute determination of the beam flux.

TPD measurements are performed by heating the sample with a 0.5 K/s linear ramp. During the TPD ramp, desorption of D_2 physisorbed on other parts of the sample manipulator and cryoshield can also occur. To reduce the influence of such background signals, desorption of D_2 from the front of the ASW surface is preferentially detected using a differentially pumped movable quadrupole mass spectrometer fitted with a Feulner cap,[48] i.e., a cone with a 3 mm aperture. During the TPD measurement the opening in the cone is moved to within 2 mm of the sample surface.

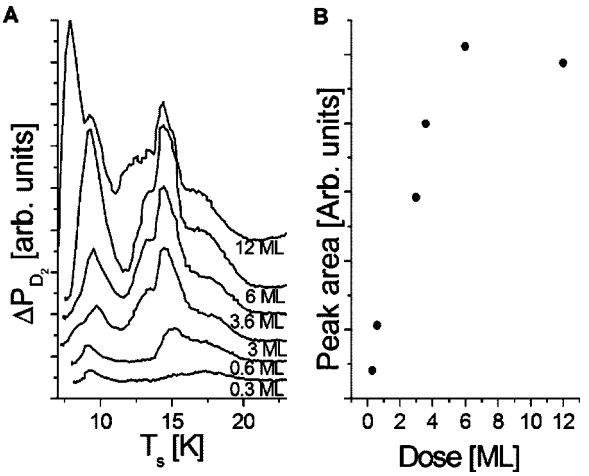

FIG. 1. (a) TPD spectra after increasing D_2 doses on a 70 ML nonporous amorphous solid water film grown at 120 K and subsequently cooled to 7 K. The employed ramp rate is 0.5 K/s. (b) Integrated signal in the high temperature peak(s) as function of dose.

III. EXPERIMENTAL RESULTS AND DISCUSSION

A. D_2 on nonporous ASW

Figure 1(a) shows a series of D_2 TPD spectra from a ~70 ML nonporous ASW film. The ASW film was grown at 120 K to insure that it was nonporous and the sample was subsequently cooled to a temperature of ~7 K prior to dosing with the D_2 molecular beam. The figure shows a sequence of TPD spectra with increasing D_2 doses. The heating rate during the subsequent TPD ramp was 0.5 K/s. At the lowest D_2 dose, a single desorption peak is observed at 17 K. At slightly higher D_2 doses, this peak shifts to lower temperatures, broadens significantly over the temperature range 12–17 K, and exhibits a partially resolved triplet structure, with an overall maxima at 15 K. As the D_2 dose is further increased, a new desorption peak appears at 9 K, and finally at the highest dose a peak begins to fill in at $T_s=8$ K.

We interpret the low dose behavior of the broad peak in the 12–17 K temperature range as due to sequential filling of a broad distribution of surface binding sites with different adsorption energies for the submonolayer of D_2 adsorbed on ASW. Initial filling of the strongest binding sites at the lowest dose gives the highest TPD temperature. The partially resolved structure of the TPD spectra suggests three different regimes of binding energies in the submonolayer, although there is no *a priori* obvious reason for this. The interpretation of sequential filling of a distribution of binding sites on the surface is confirmed by Fig. 1(b) which shows the integrated TPD signal from the 12–17 K peak as a function of D_2 dose. This saturates with dose, thereby suggesting saturation at

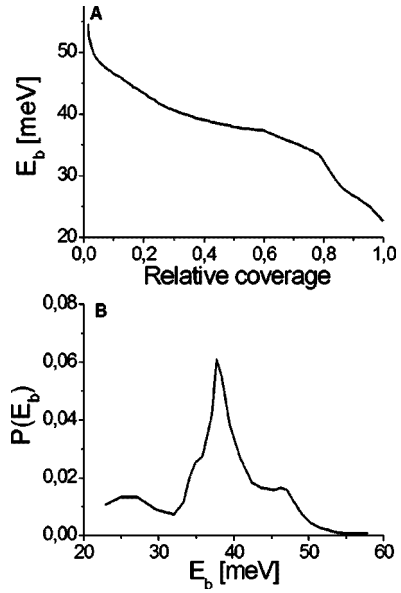

FIG. 2. (a) The binding energy as function of relative D_2 coverage on the nonporous ASW surface for the 3 ML D_2 dose shown in Fig. 1(a). (b) The D_2 population vs binding energy $P(E_b)$ on the nonporous ASW surface for the 3 ML D_2 dose shown in Fig. 1(a).

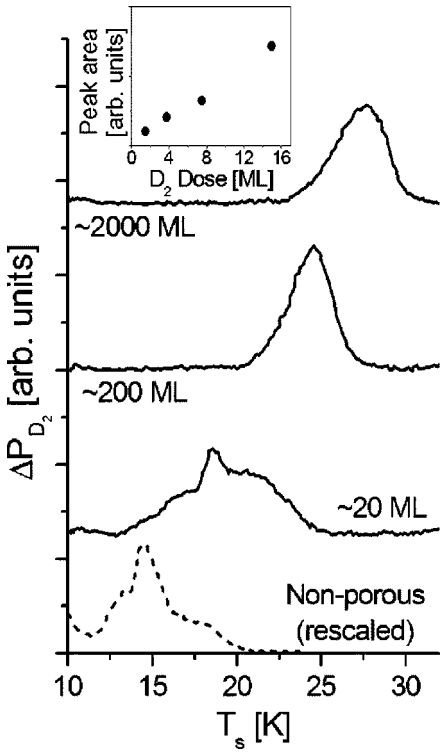

FIG. 3. TPD spectra of 1.2 ML D_2 on porous amorphous solid water films of varying thickness (solid line). A TPD spectra of 3 ML D_2 on a 70 ML nonporous amorphous solid water film (dashed line), rescaled by a factor of 0.5, is shown for comparison. The employed ramp rate is 0.5 K/s. The inset shows the integrated TPD signal after increasing D_2 doses on a 2000 ML porous amorphous solid water film.

monolayer coverages, i.e., at doses of ~6 ML. The TPD feature appearing at 9 K at higher doses is attributed to desorption of the bilayer of D_2 adsorbed on ASW. For even higher D_2 doses, the bilayer peak saturates and a TPD feature at 8 K occurs. This feature is interpreted as the desorption of multilayer D_2 and demonstrates that a surface temperature of ~7 K (Ref. 47) is obtained with our sample holder and flowing liquid He cryostat. The slopes in Fig. 1(b) represent the sticking coefficient for D_2 on the ASW and partially D_2 covered ASW surface. We see that the sticking coefficient is almost constant until ML saturation. Because of uncertainties in the absolute D_2 flux, we do not attempt to extract a value. It was measured previously, however, using the method of King and Wells to be ca. 0.2 ± 0.15.[26]

Figure 2(a) shows the binding energy as a function of relative coverage $E_b(\Theta)$ for the 3 ML D_2 dose shown in Fig. 1(a). It has been computed by assuming a preexponential factor of 10^{13} s^{-1} and inverting the Polanyi–Wigner equation, as described elsewhere.[49] The coverage in all binding sites with binding energy above a value E_b can be expressed as

$$\Theta(E_b) = \int_{E_b}^{\infty} P_b(E_b) dE_b, \tag{1}$$

where $P_b(E_b)dE_b$ is the relative population of molecules in sites with binding energy E_b. $\Theta(E_b)$ is obtained by inverting $E_b(\Theta)$ and $P_b(E_b)$ can then be computed as $-d\Theta(E_b)/dE_b$. Figure 2(b) shows the D_2 population vs binding energy $P_b(E_B)$ on the ASW surface for the 3 ML D_2 dose shown in Fig. 1(a). The binding energy distribution in the monolayer peak is seen to be rather broad ranging from approximately 35 meV to 46 meV. Note that the peak at ~25 meV arises because of the beginning buildup of the bilayer. We show in Sec. IV that a broad distribution of binding sites for monolayer adsorption of D_2 on an ASW surface is consistent with theory, and give a physical reason for this in terms of the nanoscale roughness of the surface.

B. D_2 on porous ASW

Figure 3(a) shows background subtracted D_2 TPD spectra from porous ASW films of varying thickness. The porous ASW films were grown at a sample temperature of 10 K and the film thickness range from 20–2000 ML. After film growth, a 1.2 ML D_2 dose from the molecular beam was applied. For comparison a D_2 TPD spectra after a 3 ML dose of D_2 onto a 70 ML nonporous ASW film grown at 120 K is also shown (dashed line) (the coverages in the nonporous and porous cases are comparable, since the sticking on the nonporous surface is reduced by a factor of 3 compared to the porous surface). The key observations are (1) that the D_2 TPD desorption peak shifts towards higher temperatures with increasing ASW film thickness and (2) that the peak is significantly narrowed for the thicker ASW films (200 ML and 2000 ML). For example, a relative sharp peak is observed at 28 K for the 2000 ML ASW film. This contrasts significantly with the broader peak at 12–17 K for the nonporous ASW film.

The inset in Fig. 3(a) shows the integrated TPD intensity as a function of D_2 dose for a 2000 ML porous ASW film. The integrated TPD intensity is strictly linear with dose, even for doses significantly higher than that required to saturate the nonporous ASW. This suggests that the D_2 molecules are sufficiently mobile at the dosing temperature of 10 K to re-

distribute during the D_2 dose to a larger overall surface area by surface diffusion into the pores. This explains why no evidence of bilayer or multilayer D_2 peaks was observed on the porous ASW films for any D_2 dose. The D_2 coverage relative to the total surface area of the sample (including that of the pores) is therefore below a monolayer. Again, the slope in the figure gives the sticking coefficient of D_2 onto porous ASW. Again, absolute values were not obtained for this due to uncertainties in the absolute D_2 flux. However, the ratio of sticking for porous to nonporous ASW is accurately obtained by comparing the slopes of the inset in Fig. 3(a) to that of Fig. 1(b), i.e., as a ratio of 3.0.

To ensure that the upwards shift in temperature of the TPD peak is not due to a temperature gradient or temperature lag during the TPD ramp which increases with film thickness, the TPD ramp rate was reduced by a factor of 5. The resulting TPD spectra were nearly identical to those shown in Fig. 3. They did, however, show small temperature shifts of ca. 1 K consistent with anticipated ramp rate variations assuming a Redhead analysis of first order desorption. To further confirm that there were no thermal inhomogeneities or gradients in the ASW films, we measured the multilayer N_2 peak desorption from the Cu substrate and from a 1000 ML porous ASW film grown at 10 K. These showed no observable difference in the multilayer peak desorption temperature, again indicating no surface thermal lag caused by the thick ASW film.

The qualitative effects of an upward shift and narrowing with ASW film thickness described here for D_2 TPD have also been observed with small doses of N_2 onto porous ASW films. For saturation doses of N_2, however, the overall TPD spectra simply broaden to higher temperatures with increasing porous film thickness.[10]

To explain the dependence of the D_2 TPD peak position on ASW film thickness we invoke a simple one-dimensional model in which D_2 molecules are assumed to diffuse rapidly (relative to the time scale of the TPD experiment) into the pores of the ASW film and thus become uniformly distributed on the surface of the interconnected pore structure as well as the bulk surface. We consider a one-dimensional model since $t \ll d$, where t is the film thickness and d is the beam diameter on the surface. We assume that diffusion is sufficiently rapid to cause a uniform D_2 distribution vertically in the ASW film, but not sufficiently rapid to cause significant lateral spreading. Once the D_2 molecules have diffused into the pores, thermally breaking the ASW-D_2 bond will not produce direct desorption into the gas phase. Instead the D_2 will readsorb on the pore wall. The net result is a series of desorption-readsorption events, in which the molecules perform a random walk in the porous structure until they finally reach the upper layers and are able to desorb directly into the gas phase. In this picture, the measured desorption from the sample is not proportional to the total D_2 coverage but instead to the D_2 coverage in only the top layer at the vacuum interface. The coverage in the top layer Θ_s for a N_l monolayer thick ASW film with porosity ξ_{por} is then given by $\Theta/(1+N_l\xi_{por})$, where Θ is the total D_2 dose adsorbed on the surface. The coverage in the pores is in turn given by $\Theta N_L \xi_{por}/(1+N_l\xi_{por})$. Assuming fast diffusion and a uniform D_2 distribution throughout the film then leads to the following modification of the Polanyi–Wigner expression for the D_2 desorption rate for a single fixed binding energy E_b of D_2 on the surface:

$$\frac{d\Theta}{dt} = -k_0 e^{-E_b/k_B T_s}\Theta_s = -k_0 e^{-E_b/k_B T_s}\frac{1}{1+N_l\xi_{por}}\Theta, \qquad (2)$$

where k_0 is the preexponential factor, k_B is the Boltzmann constant, and T_s is the surface temperature.

This simple model predicts an upwards shift in the TPD peak with increasing ASW film thickness since the prefactor scales as $\propto 1/(1+N_l\xi_{por})$. However, one major limitation of this simple model is that it does not take the distribution of binding energies of D_2 on the ASW film into account. Figure 2(b) shows that D_2 adsorbs into a rather broad distribution of binding energies on the nonporous ASW surface. For the porous ASW films we also expect a broad distribution of binding energies. Furthermore, we expect this distribution to be affected by the porosity in two ways. First, because of the porous nature of the film the total number of available binding sites is increased, including the number of high energy binding sites. Hence for the thicker films a relatively larger fraction of the D_2 adsorption occurs into high energy binding sites. Second, binding sites in the pores could have higher binding energy than sites on the nonporous surface.

By inverting the modified Polanyi–Wigner equation above and following the same procedure as in the nonporous case we obtain the relative D_2 population vs binding energy for the 1.2 ML D_2 dose on 20 ML porous ASW shown in Fig. 3(a). The result is shown in Fig. 4(b). Figure 4(a). shows $E_{b,20\ ML}(\Theta)$). As can be seen binding energies ranging from 45 meV to 59 meV are mainly populated at this dose. Hence we do indeed see increased binding energies in the pores as compared to the distribution on the nonporous surface, the dashed line. In Sec. IV we try to give a physical reason for this shift in binding energies in terms of the degree of coordination between adsorbed D_2 molecules and water molecules in the pores relative to those on the ASW surface. It should be pointed out that there may be an additional lower energy tail to the porous E_b distribution that is not probed by this TPD since those sites are not filled in the 1.2 ML D_2 dose on 20 ML porous ASW.

Based on the distribution found in Fig. 4 and the modified Polanyi–Wigner equation we can now compute simulated TPD spectra for a 1.2 ML D_2 dose on 20, 200, and 2000 ML ASW films. To approximate the effect of increased number of available sites with increasing ASW film thickness, we use $E_{b,N_l}(\Theta) = E_{b,20\ ML}[\Theta(1+20\xi_{por})/(1+N_l\xi_{por})]$. The simulated spectra are shown in Fig. 5(a).

The very good quantitative agreement obtained between the model and the experimental data is somewhat fortuitous, since the high energy tail of the binding energy distribution is very dependent on background subtraction and since the exact porosity of the ASW film is uncertain. However, independent of the exact choice of parameters the simulations will nicely recreate the same trends as the experimental data, i.e., the upwards shift in temperature and the narrowing of the desorption peaks with film thickness. The experimental observations can therefore be explained as being the result of

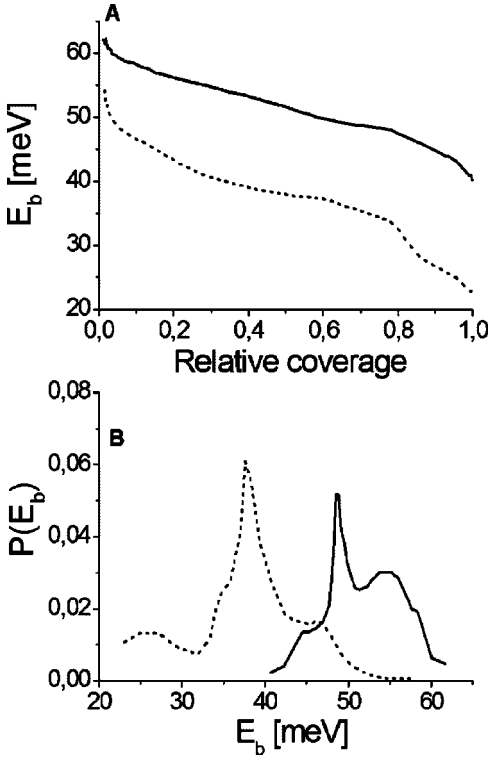

FIG. 4. (a) The binding energy as function of relative D_2 coverage on the 20 ML porous ASW surface for the 1.2 ML D_2 dose shown in Fig. 3(a) (solid line) and on the nonporous ASW surface for the 3 ML D_2 dose shown in Fig. 1(a) (dashed line). (b) The D_2 population vs binding energy $P(E_b)$ on the 20 ML porous ASW surface for the 1.2 ML D_2 dose shown in Fig. 3(a) (solid line) and on the nonporous ASW surface for the 3 ML D_2 dose shown in Fig. 1(a) (dashed line).

(1) fast diffusion into the pores causing a uniform distribution of D_2 all through the film, (2) a reduction in desorption rate due to the fact that only desorption from the top layers of the ASW film leads to release of D_2 molecules into the gas phase, (3) the availability of higher energy binding sites in the pores than on the nonporous surface, and (4) an increase in available binding sites, leading to an increased population of D_2 molecules in high energy binding sites, with increasing ASW film thickness.

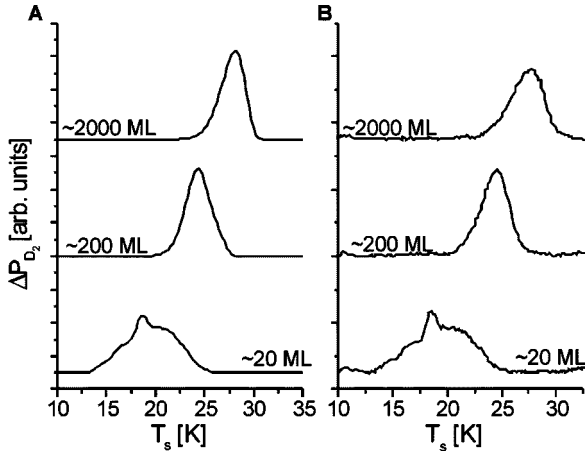

FIG. 5. (a) Simulated TPD spectra for ASW films of varying thickness based on the binding energy distribution derived from the D_2 TPD from the 20 ML ASW film shown and computed using the modified Polanyi–Wigner equations as described in the text. (b) The TPD spectra displayed in Fig. 2 reproduced for comparison.

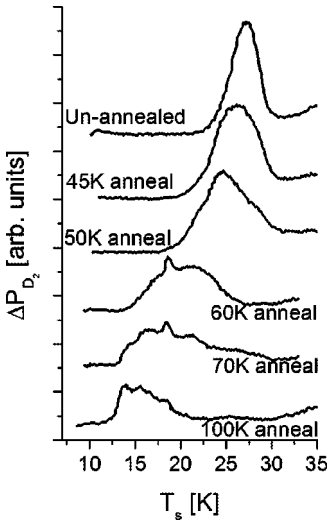

FIG. 6. TPD spectra of 1.2 ML of D_2 from ~2000 ML ASW films grown at 10 K and subsequently annealed to the stated temperatures. The employed ramp rate is 0.5 K/s.

C. Effects of thermal anneals

Figure 6 shows the D_2 TPD spectra from a 2000 ML ASW film grown at 10 K and then subsequently thermally annealed for 1 min at the various temperatures given in the figure. After the anneal the ASW films are again cooled to a temperature of 10 K for D_2 dosing. As can be seen, anneals to higher temperatures result in a downwards shift in temperature of the TPD peak. We interpret this change as implying that the main effect of thermal anneals visible in the TPD is a reduction of the ASW film porosity and a reduction of available high energy binding sites due to pore collapse caused by the enhanced H_2O mobility. After anneals to temperatures of 100 K or above, the TPD spectra look similar to those obtained when dosing D_2 on ASW films grown at 120 K, i.e., the ASW film porosity and the higher energy binding sites are essentially gone. The interpretation that the main effect of thermal annealing is a reduction in porosity and in the number of available high energy binding sites is in good agreement with previous results obtained from ASW film density measurements,[3,50] effective surface area measurements,[10] and IR measurements of dangling O–H bonds.[13,30,51] The reduction in porosity and high energy binding sites is expected to be paralleled by a transition from the high density to the low density phase.[8] However, we have not been able to identify any unique signs of this high to low density transition in the TPD spectra beyond what is anticipated from the reduction in porosity.

Figure 6 also shows that no dramatic reduction of porosity occurs for thermal anneals of ~45 K. This explains why both H_2 and N_2, which are desorbing at temperatures below 20 K and 45 K, respectively, are able to desorb from ASW films of up to a few thousand monolayers before severe ASW film restructuring and pore collapse sets in.

For CCl_4,[31,34,35] methane,[14] and CO (Ref. 33) that bind more tightly to the ASW surface, considerably more complex behavior is observed since the ASW structure has already undergone considerable restructuring at the higher temperatures needed to desorb these species.

IV. THEORETICAL CALCULATIONS OF H_2-ASW BINDING ENERGY DISTRIBUTIONS

To simulate the adsorption of H_2 to ASW and crystalline ice, classical trajectory (CT) calculations have been performed. Once H_2 equilibrates on the surface, its potential energy E_b is calculated. The sticking procedure insures that a proper statistical weighting of the molecules adsorbed on the surface is obtained. Essentially, we have followed the same approach as used before to study the sticking of CO to crystalline and amorphous ice.[39] Some details of the method as applied to H_2–ice are presented below.

A. The ice surfaces

The ASW and crystalline ice surfaces were prepared essentially in the same way as the surfaces used previously to study the adsorption of CO to ice,[39] using the molecular dynamics (MD) method.[52] The crystalline surface was modelled by four bilayers containing 240 moving water molecules. The ASW film consists of six bilayers containing 360 moving water molecules. The moving bilayers in both the ice films were superimposed on two bilayers of 120 fixed water molecules. The moving water molecules were treated as rigid rotors, but were otherwise allowed to move according to Newton's equations of motion. Periodic boundary conditions were applied in the *xy* plane, parallel to the scattering plane, to simulate an infinite surface. The TIP4P pair potential[53] was used to describe the water-water interactions. The initial ice configurations obey the ice rules[54] and has a zero dipole moment.

The ASW film was equilibrated at the desired temperature (T_s=90 or 10 K) in a stepwise fashion. Starting from an ice Ih configuration at T_s=10 K, the surface was first heated to and equilibrated at T_s=300 K, and then the temperature was abruptly decreased and equilibrated at T_s=90 or 10 K. In the surface equilibration, a time step of 1 fs was used. The method used here to prepare the amorphous ice surface is similar to the fast quenching method used to simulate amorphous ice by Essmann and Geiger.[19] The crystalline ice film was equilibrated at T_s=90 K.

In the case of crystalline ice, the surface was operationally defined to be at a height equal to Z=22.5 Å. However, because of the roughness of the ASW surface, the position of the surface-vacuum interface is ill defined. The Z coordinates of the water molecules on top at the surface-vacuum interface vary from about 23 to 30 Å (relative to the bottom of the slab, defined to be at 0 Å). Although the ASW ice surface is quite rough with the presence of several hills and valleys, it does not exhibit any true nanoscale pore strucure (this might be due to the size of the simulated unit cell). However, some surface pores are larger than the hexagonal rings of diameter of about 4.5 Å. We suspect that the simulated ASW surface is rougher than the non-porous ASW surface used in the experiments. Thus, we believe that the simulated ASW surface is somewhat intermediate between the porous and nonporous surfaces used in the experiments.

B. H_2–ice interaction

In the CT calculations, the H_2-ice interaction has been constructed as a sum of H_2-H_2O pair potentials. The H_2-H_2O pair potential is the same pair potential as developed by Zhang *et al.*[55] as a fit to electronic structure calculations at the MP4 level of theory, and used later to simulate the interaction between H_2 and amorphous water ice clusters.[37] The interaction has the form

$$V_{H_2-H_2O} = \sum_{i,j} \frac{q_i q_j}{r_{ij}} + \sum_k LJ_k(8-6). \tag{3}$$

The H_2O-H_2O and H_2-H_2O interactions were set to zero at very long distances ($\geqslant$10 Å) using a switching function.[56]

C. Molecular dynamics simulations

The initial orientation and the impact position of the impinging H_2 on the surface were selected at random using the Monte Carlo technique.[57] The initial rotational energy of H_2 was set to zero. The calculations of 100 trajectories were performed at normal incidence (θ_i=0), at incidence energy E_i=10 meV. Each trajectory was run for 11 ps, using a time step of 1/9 fs. At the beginning of each trajectory, H_2 was placed 11.3 Å above the crystalline ice surface or above the highest portion of the ASW ice slab, with a momentum directed at the surface. H_2 was then considered to be in the gas phase, infinitely far away from the ice surface. To simulate the collision dynamics, Newton's equations of motion of the impinging H_2 and the water molecules were integrated using an improved leapfrog algorithm.[58] Sticking of H_2 was defined to occur as more than one turning point is exhibited in the Z coordinate of H_2 for motion normal to the surface, and the final energy E_f of H_2 interacting with the ice surface is less than kT_s(E_f<−8 meV). Here, E_f of the adsorbed molecule is the sum of its potential, translational, and rotational energy. The zero of the potential energy is defined by H_2 being in the gas phase. In the case of sticking, $Z_f \leqslant$26.5 Å when adsorbed to the crystalline surface and $Z_f \leqslant$32.5 Å when adsorbed to the ASW surface, where Z_f is the final value of the Z coordinate of H_2 at the end of the trajectory for motion normal to the surface. The second possibility is scattering when H_2 returns to the gas phase ($Z_f \geqslant$29.5 Å for the case of crystalline ice and $Z_f \geqslant$40.0 Å for the case of the ASW ice).

V. RESULTS AND DISCUSSION

Analysis of the trajectories shows that after the impact with the surface, some of the H_2 collision energy normal to the surface is converted to motion parallel to the surface due to the roughness of the ice surface. This parallel motion is quenched by subsequent trapping into adsorbing wells as the molecule equilibrates with the surface. At T_s=90 K, H_2 shows considerable diffusive motion to nearby adsorbing wells during the MD simulation of the individual trajectories for both amorphous and crystalline ice; i.e., it remains trapped in a well for some time and then jumps to an adjacent well where it is trapped for a period and so on. There-

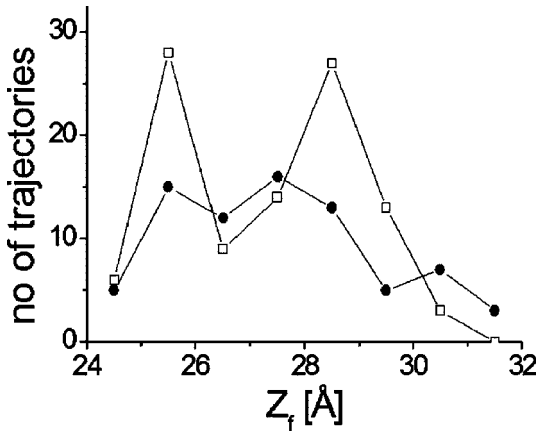

FIG. 7. The number of adsorbing trajectories plotted as a function of Z_f, for H_2 adsorbed to amorphous ice, at $T_s=90$ K (black dots) and at $T_s=10$ K (open squares), with $E_i=10$ meV and for normal incidence.

fore only the trajectories that satisfy both conditions on E_f and Z_f are considered to be sticking trajectories.

The calculations show that the excess mobility gained immediately after impact with the surface, from converting perpendicular momentum into parallel momentum, is damped out within a few picoseconds, limiting the movement of the molecules to ~10 Å. The experiments show that the adsorbed D_2 samples the entire depth ($>10^3$ Å) of the porous network in the ASW films. Hence the excess mobility immediately after impact—the "hot molecule" effect—cannot be the dominant cause of the mobility into the pores observed in the experiments. This long time mobility can only be caused by diffusion.

For the thermal E_i considered here (10 meV), the computed sticking probability of H_2 is 0.78 ± 0.05 for both ASW and crystalline ice at $T_s=90$ K. However, the sticking probability to the ASW ice is unity at $T_s=10$ K. The calculated values are higher than those measured experimentally for D_2 (0.2 ± 0.15 for the nonporous ASW and 0.6 ± 0.1 for the porous ASW at $T_s=10$ K).[26] The discrepancy between the calculated and the measured values of the sticking probabilities can be caused by several factors. First, the sticking probability found experimentally was measured using a thermal D_2 beam of $E_i=25$ meV (300 K) instead of 10 meV and is undoubtedly lower at higher E_i: CT calculations predict a similar sticking probability to the measured one at $E_i=100$ meV. Lower values of E_i were considered in the calculations to obtain a reasonable statistics in the calculations of the binding energy distributions of H_2. Second, the calculations presented here are classical and hence neglect elastic scattering that limits sticking. Third, as will be discussed later, the calculated binding energy of H_2 is overestimated. However, since our principal motivation is to understand the binding energy distributions, we have not looked into this disagreement in any detail.

Figure 7 shows the number of sticking trajectories distributed as a function of the the final height of H_2 at the end of the trajectories, where $Z=0$ is defined at the bottom of the ASW simulated ice slab for the two surface temperatures. The distributions show the presence of at least two preferential adsorption sites: at high values of $Z(\geqslant 26.5$ Å), where H_2 is adsorbed at the surface hills and a second regime at low values of $Z(\leqslant 26.5$ Å), where the sticking occurs at the surface valleys. The simulations also show that for both ASW and crystalline ice films there is no penetration of the surface upon collision by any H_2.

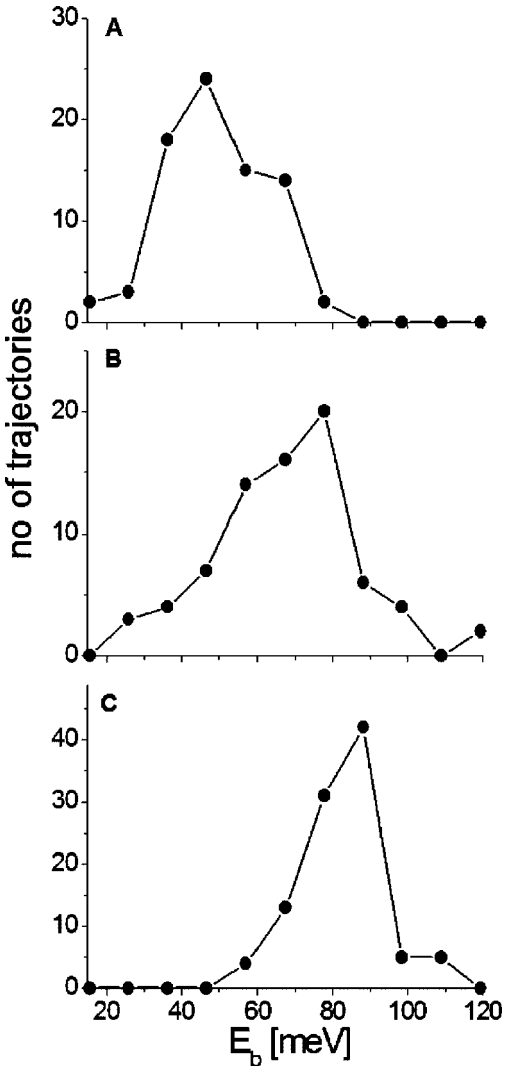

FIG. 8. The number of adsorbing trajectories plotted as a function of E_b, for H_2 adsorbed to (a) crystalline ice at $T_s=90$ K, (b) amorphous ice at $T_s=90$ K, and (c) amorphous ice at $T_s=10$ K.

The binding energy of H_2 in a given sticking CT is obtained from Eq. (2) summed over the water molecules close to H_2, within a sphere of radius of 10 Å centered at the center of mass of H_2. In Fig. 8 the number of adsorbing trajectories is distributed over E_b of H_2. Figures 8(a) and 8(b) show the distribution for a 90 K crystalline ice surface and a 90 K ASW surface, respectively. As can be seen the distribution for the ASW surface (rough and corrugated) is broadened and shifted towards higher values of E_b compared to the case of crystalline ice (smooth). The broadening of the calculated E_b distribution on the ASW surface suggests different H_2 coordinations for different adsorption wells; i.e., the number of water molecules interacting with H_2 differs from one adsorption site to another. This is confirmed by considering the dependence of E_b on the final Z value of H_2 (Z_f). Figure 9 shows E_b plotted as a function of Z_f. The figure shows that

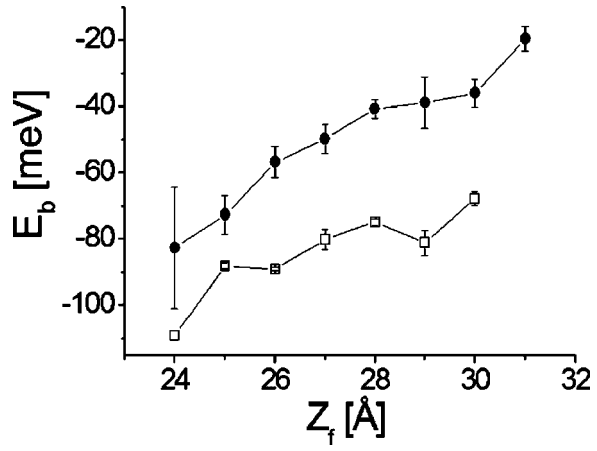

FIG. 9. The binding energy of H_2, E_b, plotted as a function of Z_f, for H_2 adsorbed to amorphous ice, at T_s=90 K (black dots) and at T_s=10 K (open squares).

E_b decreases with Z_f, similar to the case of CO interacting with ASW ice, which was also explained by the coordination of CO.[40]

Figure 9 demonstrates that binding energies of H_2 bound in surface valleys are higher than those of H_2 bound on surface peaks (surface hills). We have computed the average binding energy of H_2 for both adsorbing regimes discussed above for $\geqslant$26.5 Å (surface hills) and $\leqslant$26.5 Å (surface valleys) and found $\langle E_b \rangle = 61 \pm 2$ meV(77 ± 1 meV) for the upper portion of the surface and 84 ± 2 meV(94 ± 1 meV) for the lower portion of the ASW surface at T_s=90 K(10 K). In surface valleys, H_2 is expected to interact with a larger number of water molecules compared to H_2 adsorbed to a surface hill, which leads to a stronger binding to the surface. This result is in agreement with the results of the calculations of Hixson *et al.*[37] The computed binding energy of H_2 adsorbed on the top portion of the ASW ice is similar to the $\langle E_b \rangle$ of H_2 adsorbed to crystalline ice.

Figures 8(b) and 8(c) show the binding energy distributions of H_2 adsorbed to ASW ice at T_s=90 and 10 K, respectively. The distribution at T_s=10 K is narrower and peaks at a higher binding energy than the distribution at T_s=90 K. The differences in distributions is caused by the extra energy available at 90 K. By equipartition this extra energy will lead to population of nonzero hindered translational and rotational modes of the H_2 molecule on the surface. Also, at high T_s H_2 diffuses rapidly and we anticipate that the molecules ultimately populates all wells at the end of the CT according to the thermal distribution of the binding energies. For the surface at T_s=10 K, the H_2 diffusive motion is still possible but is slower and the molecules are primary trapped in high binding energy wells.

For the crystalline ice at T_s=90 K an average value of the final potential energy E_b at the end of the trajectories of $\langle E_b \rangle = 49 \pm 1$ meV was found. For ASW ice, $\langle E_b \rangle$ was found to be 68 ± 1 and 83 ± 2 meV at T_s=90 and 10 K, respectively. These dynamic results obtained from the MD calculations compare well with earlier calculations obtained for H_2 interacting with a static amorphous water cluster.[37] The maximum of E_b of H_2 was calculated for 240 different adsorption wells. Those results are more comparable with our results obtained at high T_s(90 K), as H_2 ultimately occupies all wells at the end of the CT according to the thermal distribution of the binding energies as discussed above. In the calculations of Hixson *et al.*, an average E_b of 63 meV was obtained, in good agreement with our results. The maxima were found to be in the range between 26 and 121 meV, also in a good agreement with our findings here [see Fig. 8(b)].

To compare the calculations with the experimental results we have to consider the nature of the studied surfaces. Both calculations and experiments have considered two types of water ice surfaces differing in degree of corrugation. Of these surfaces the crystalline ice surface is of course the smoothest. Of the two experimental surfaces the nonporous one should be the least corrugated. As stated earlier the simulated ASW surface is expected to be more corrugated than the experimental nonporous ASW surface. The experimental porous ASW surface on the other hand is of course quite corrugated on the nanometer scale, due to the porosity, however, it is unclear how the corrugation on the subnanometer scale compares to that of the simulated ASW surface. Hence we would expect the binding energies of the nonporous ASW surface to lie between the calculated binding energies found for the crystalline ice and the ASW, while the binding energies for the porous surface are expected to be closer to the calculated binding energies for the ASW surface.

The theoretical calculations were made for H_2 while the experiments were performed using D_2. Hence to compare the values found in the two cases an estimated zero point energy of ca. 6 meV has to be added to the calculated E_b to compare with the experimental value. The calculated average binding energy for the crystalline ice with the $\sim$6 meV zero point energy added is $\langle E_{b,D_2} \rangle = 55 \pm 1$ meV, which should be compared to the estimated maximum binding energy value (46 meV) of D_2 from the TPD experiments of the nonporous ASW, see Fig. 2(b). At low coverage these high energy binding sites are preferentially populated, see the 0.3 ML dose in Fig. 1(a). However, since we would expect the H_2 molecules to populate more or less the full distribution of binding energies at 90 K, due to thermal diffusion, the calculated average binding energy for H_2 on crystalline ice seems surprisingly high. Especially since the crystalline ice surface is thought to be less corrugated than the experimental nonporous ASW surface and hence should mainly exhibit low energy binding sites due to the lack of high coordinated valley adsorption sites, see Fig. 9. For ASW ice the zero point corrected average binding energies were found to be $\langle E_{b,D_2} \rangle = 74 \pm 1$ and 89 ± 2 meV at T_s=90 and 10 K, respectively. The calculated values are noticeably higher than those measured experimentally. For the 20 ML porous ASW surface a binding energy of 89 meV would give rise to a desorption peak at as high a temperature as 35 K. Hence, in all three cases the calculations seem to overestimate the binding energies. Presumably, this overestimate of E_b is due to the simplified model used to describe the H_2–H_2O interaction potential.

However, qualitatively the calculated binding energy distributions compare well with experiments. At T_s=10 K, Fig. 8(c) suggests that at the binding energy distribution mainly shows a single peak structure, similar to that found in

the TPD spectra for the nonporous as well as the porous ASW surface at low D_2 coverage, see the 0.3 ML dose in Fig. 1 and the traces for 200 ML and 2000 ML porous ASW ice in Fig. 3. At $T_s = 90$ K where the molecules sample more of the binding site distribution a much broader distribution of binding energies are found, see Fig. 8(b), in good agreement with the experimental observations for the case of the nonporous and the 20 ML porous ASW ice at higher coverages, see Figs. 1(a) and 3(a). Figure 8(b) even suggests that the binding energy distribution shows multiple peak structure, however, in the calculations we did not obtain sufficient statistics to follow this more closely. The broad distribution of binding energies were associated with the existence of binding sites of varying coordination. H_2 molecules adsorbed in surface valleys were seen to be more strongly coordinated and hence more strongly bound than H_2 molecules adsorbed on surface hills or on the flat crystalline ice surface, see Fig. 9. Due to this effect the calculations also show an increase and a broadening in binding energies with increasing surface corrugation, compare Figs. 8(a) and 8(b). Likewise in experiments we observe a dramatic increase in binding energy when going from the relatively smooth nonporous ASW surface to the more corrugated porous ASW surface, see Fig. 4(b). This indicates that the binding energy of H_2 in the pores is indeed higher (H_2 is more strongly bound) than when it is adsorbed on top of the ice surface and leads us to believe that this is due to the fact that binding sites of higher coordination exists in the pores than on the nonporous surface.

The presented experiments include data from ASW films in both the high density (10 K grown ASW), low density (120 K grown ASW), and mixed (annealed ASW) phases. In the analysis and discussion this aspect has not been stressed. This is due to the fact that we see no discernible influence of the distinct phases in our data. While we cannot rule out that such an influence might exist, it seems to be well masked by the effects brought about by the different morphologies or porosities of the ASW films. Hence, we are convinced that the porosity, rather than the phase (high density or low density) of ASW films play the dominant role in determining the desorption kinetics of physisorbed species on the ASW surface.

VI. CONCLUSIONS AND ASTROCHEMICAL IMPLICATIONS

Using TPD we have measured the broad distribution of binding energies of D_2 adsorbed on nonporous and porous ASW film surfaces and have shown that D_2 is more strongly bound on the porous ASW surface. For porous ASW films we have shown how the TPD peak narrows and shifts towards higher temperatures with increasing film thickness. We have developed a simple 1D diffusion model which can qualitatively explain this behavior. The model assumes fast D_2 diffusion throughout the porous ASW film structure. The TPD peak shift towards higher temperature with increasing thickness is then mainly ascribed to two effects. (1) Since desorption into the gas phase can only occur for molecules in the top layer of the film, the D_2 desorption rate is reduced by a film thickness and porosity dependent factor. (2) Due to the broad distribution of binding energies on the porous surface an increase in ice thickness with the resulting increase in effective surface area and hence also in available high energy binding sites results in a relative increase in the population of D_2 molecules occupying these sites that leads to a further upwards shift of the TPD peaks. All experiments described in this paper were performed on ASW films. However, effects (1) and (2) described above are not dependent on the detailed chemical structure of the porous material but only on its morphology. Hence, similar effects should be observable in other systems of physisorbed species on nanoporous material. Somewhat similar desorption kinetics have indeed been observed in investigations of Xe desorption from single-wall carbon nanotube bundles.[59] Our experiments also show that thermal annealing of porous ASW films results in a downwards shift in TPD peak positions, interpreted as a reduction in ASW film porosity and in the number of high energy binding sites. Finally, we have presented theoretical calculations which confirm that H_2 adsorb on the nonporous ASW surface with a distribution of binding energies. This distribution was seen to arise as a consequence of a variation in the number of water molecules interacting with the adsorbed H_2, i.e., a variation in the coordination of the adsorbed H_2. The theoretical simulations showed that H_2 adsorbed in well coordinated surface sites in surface valleys is more strongly bound than H_2 adsorbed in less well coordinated sites on surface peaks. This also implies that $H_2(D_2)$ adsorbs in nanoscale pores with higher binding energies than at the surface, in good agreement with the experimental observations.

The presented results have astrophysical implications and show that to understand surface reactions on interstellar grains a knowledge of grain surface morphology is required. In dense interstellar clouds grains are believed to be covered with icy mantles. We have measured the binding energy distribution of D_2 on the ASW film surface and have shown how the desorption rate of weakly bound species such as H_2, HD, D_2, and to some extent N_2 depend on the ASW film morphology and thickness. For porous ASW films the residence time of weakly bound species is increased with the thickness and porosity of the ASW film. These results are of particular importance when discussing the formation of molecular hydrogen in interstellar clouds. We have shown elsewhere that the morphology of interstellar grains will highly influence the formation of molecular hydrogen, the most abundant molecule in the interstellar medium. If the icy mantles on interstellar grains are porous or if the grains themselves exhibit nanometer scale porosity then the majority of H_2 molecules formed on the grains will be retained in the porous structure.[26] To correctly calculate the rate at which these molecules will subsequently desorb and return to the gas phase the effects of porosity has to be taken into account. In conclusion, to satisfactorily model the adsorption and desorption, as well as the catalysis of adsorbed molecules on dust grain surfaces, not only the chemical nature of the dust grain surface, but also its morphology has to be taken into account.

ACKNOWLEDGMENTS

This work was supported by The Danish National Research Council under Grant No. 21000269. L.H. acknowl-

edges support from the Carlsberg Foundation. A.Al-H. was supported by a Spinoza grant from the Netherlands Organization for Scientific Research (NWO) and by EEC grant RGCCWT. A.Al-H. thanks Geert-Jan Kroes for the fruitful discussion and for providing the authors with the MD code developed in the group and acknowledges The National Computing Facilities Foundation (NCF) for a generous grant of computing time. B.D.K. was supported by the U.S. Department of Energy (DOE) Office of basic Energy Sciences, Chemical Sciences Division. Pacific Northwest National Laboratory is operated for the U.S. DOE by Battelle under Contract No. DE-AC06-76RLO 1830.

[1]D. Olander and S. A. Rice, Proc. Natl. Acad. Sci. U.S.A. **69**, 98 (1972).
[2]R. S. Smith and B. D. Kay, Nature (London) **398**, 788 (1999).
[3]E. Mayer and R. Pletzer, Nature (London) **319**, 298 (1986).
[4]P. Jenniskens, D. F. Blake, M. A. Wilson, and A. Porhorille, Astrophys. J. **455**, 389 (1995).
[5]O. Mishima, L. D. Calvert, and E. Whalley, Nature (London) **310**, 393 (1984).
[6]E. Mayer, J. Appl. Phys. **58**, 663 (1985).
[7]A. H. Narten, C. G. Venkatesh, and S. A. Rice, J. Chem. Phys. **64**, 1106 (1976).
[8]P. Jenniskens and D. F. Blake, Science **265**, 753 (1994).
[9]K. P. Stevenson, G. A. Kimmel, Z. Dohnalek, R. S. Smith, and B. D. Kay, Science **283**, 1505 (1999).
[10]G. A. Kimmel, K. P. Stevenson, Z. Dohnalek, R. S. Smith, and B. D. Kay, J. Chem. Phys. **114**, 5284 (2001).
[11]G. A. Kimmel, Z. Dohnalek, K. P. Stevenson, R. S. Smith, and B. D. Kay, J. Chem. Phys. **114**, 5295 (2001).
[12]P. Parent, C. Laffon, C. Mangeney, F. Bournel, and M. Tronc, J. Chem. Phys. **117**, 10842 (2002).
[13]B. Rowland and J. P. Devlin, J. Chem. Phys. **94**, 812 (1991).
[14]N. Horimoto, H. S. Kato, and M. Kawai, J. Chem. Phys. **116**, 4375 (2002).
[15]Z. Dohnalek, G. A. Kimmel, R. L. Ciolli, K. P. Stevenson, R. S. Smith, and B. D. Kay, J. Chem. Phys. **112**, 5932 (2000).
[16]A. Bar-Nun, J. Dror, E. Kochavi, and D. Laufer, Phys. Rev. B **35**, 2427 (1987).
[17]A. I. Kolesnikov, J.-C. Li, S. Dong, I. F. Bailey, R. S. Eccleston, W. Hahn, and S. F. Parker, Phys. Rev. Lett. **79**, 1869 (1997).
[18]Q.-B. Lu, T. E. Maddey, L. Parenteau, F. Weik, and L. Sanche, Chem. Phys. Lett. **342**, 1 (2001).
[19]U. Essmann and A. Geiger, J. Chem. Phys. **105**, 4678 (1995).
[20]Q. Zhang and V. Buch, J. Chem. Phys. **92**, 5004 (1990).
[21]V. Buch, J. Chem. Phys. **93**, 2631 (1990).
[22]V. Buch and J. P. Devlin, J. Chem. Phys. **94**, 4091 (1991).
[23]G. Manico, G. Raguni, V. Pironello, J. Roser, and G. Vidali, Astrophys. J. **548**, L253 (2001).
[24]J. Roser, G. Vidali, G. Manico, and V. Pironello, Astrophys. J. **555**, L61 (2001).
[25]J. Roser, G. Manico, V. Pironello, and G. Vidali, Astrophys. J. **581**, 276 (2002).
[26]L. Hornekær, A. Baurichter, V. Petrunin, D. Field, and A. C. Luntz, Science **302**, 1943 (2003).
[27]J. Takahashi, K. Masuda, and M. Nagaoka, Astrophys. J. **520**, 724 (1999).
[28]J. Takahashi, K. Masuda, and M. Nagaoka, Mon. Not. R. Astron. Soc. **306**, 22 (1999b).
[29]A. Bar-Nun, G. Herman, D. Laufer, and M. L. Rappaport, Icarus **63**, 317 (1985).
[30]B. Rowland, M. Fisher, and J. P. Devlin, J. Chem. Phys. **95**, 1378 (1991).
[31]R. S. Smith, C. Huang, E. K. L. Wong, and B. D. Kay, Phys. Rev. Lett. **79**, 909 (1997).
[32]P. Ayotte, R. S. Smith, K. P. Stevenson, Z. Dohnalek, G. A. Kimmel, and B. D. Kay, J. Geophys. Res. **106**, 33387 (2001).
[33]M. P. Collings, J. W. Dever, H. J. Fraser, M. R. S. McCoustra, and D. A. Williams, Astrophys. J. **583**, 1058 (2003).
[34]V. Sadtchenko, K. Knutsen, C. F. Giese, and W. R. Gentry, J. Phys. Chem. B **104**, 2511 (2000).
[35]V. Sadtchenko, K. Knutsen, C. F. Giese, and W. R. Gentry, J. Phys. Chem. B **104**, 4894 (2000).
[36]V. Buch and Q. Zhang, Astrophys. J. **379**, 647 (1991).
[37]H. G. Hixson, M. J. Wojcik, M. S. Devlin, J. P. Devlin, and V. Buch, J. Chem. Phys. **97**, 753 (1992).
[38]K. Masuda, J. Takahashi, and T. Mukai, Astron. Astrophys. **330**, 773 (1998).
[39]A. Al-Halabi, E. F. van Dishoeck, and G. J. Kroes, J. Chem. Phys. **120**, 3358 (2004).
[40]A. Al-Halabi, H. J. Fraser, G. J. Kroes, and E. F. van Dishoeck, Astron. Astrophys. **422**, 777 (2004).
[41]N. Watanabe, T. Horii, and A. Kouchi, Astrophys. J. **541**, 772 (2000).
[42]A. G. G. M. Tielens and W. Hagen, Astron. Astrophys. **114**, 245 (1982).
[43]L. B. D'Hendecourt, L. J. Allamandola, and J. M. Greenberg, Astron. Astrophys. **152**, 130 (1985).
[44]A. Jones and D. Williams, Mon. Not. R. Astron. Soc. **209**, 955 (1984).
[45]W. Hagen, A. G. G. M. Tielens, and J. M. Greenberg, Chem. Phys. **56**, 367 (1981).
[46]L. Diekhoner, H. Mortensen, A. Baurichter, and A. C. Luntz, J. Chem. Phys. **115**, 3356 (2001).
[47]H. Schlichting and D. Menzel, Rev. Sci. Instrum. **64**, 2013 (1993).
[48]P. Feulner and D. Menzel, J. Vac. Sci. Technol. **17**, 662 (1980).
[49]Z. Dohnalek, G. A. Kimmel, S. A. Joyce, P. Ayotte, R. S. Smith, and B. D. Kay, J. Phys. Chem. B **105**, 3747 (2001).
[50]Z. Dohnalek, G. A. Kimmel, P. Ayotte, R. S. Smith, and B. D. Kay, J. Chem. Phys. **118**, 364 (2003).
[51]G. Ritzhaupt, N. Smyrl, and J. P. Devlin, J. Chem. Phys. **64**, 435 (1976).
[52]R. N. Porter and L. M. Raff, *Dynamics of Molecular Collisions, Part B* (Plenum, New York, 1976).
[53]W. L. Jorgensen, J. Chandrasekhar, J. D. Madura, R. W. Impey, and M. L. Klein, J. Chem. Phys. **79**, 926 (1983).
[54]J. D. Bernal and R. H. Fowler, J. Chem. Phys. **1**, 515 (1933).
[55]Q. Zhang, L. Chenyang, Y. Ma, F. Fish, M. M. Szczesniak, and V. Buch, J. Chem. Phys. **96**, 6039 (1992).
[56]G. J. Kroes and D. C. Clary, J. Phys. Chem. **96**, 7079 (1992).
[57]M. P. Allen and D. J. Tildesley, *Computer Simulations of Liquids* (Clarendon, Oxford, 1987).
[58]D. Fincham, Mol. Simul. **8**, 165 (1992).
[59]H. Ulbricht, J. Kriebel, G. Moos, and T. Hertel, Chem. Phys. Lett. **363**, 252 (2002).